BUTTERWORTH HEINEMANN

*Polymer* Vol. 36 No. 9, pp. 1743–1759, 1995
Elsevier Science Ltd
Printed in Great Britain

# Experimental high-resolution electron microscopy of polymers*

**David C. Martin**†
*Materials Science and Engineering, and the Macromolecular Science and Engineering Center, The University of Michigan, 2022 H. H. Dow Building, Ann Arbor, MI 48109-2136, USA*

**and Edwin L. Thomas**
*Materials Science and Engineering, and the Program in Polymer Science and Technology, Massachusetts Institute of Technology, Cambridge, MA 02139, USA*

High-resolution imaging of ordered polymers is described both theoretically and experimentally. The relationship between the actual three-dimensional specimen structure and the resultant two-dimensional image intensity distribution is developed using the multislice formalism. The influence of the electron optical conditions on the image is demonstrated with experimental data, as well as with image simulations. Practical details of specimen preparation, as well as the effects of specimen structural defects on the image, are presented. A significant challenge for polymer microscopists is to minimize the deleterious effects of electron beam damage and to identify image artifacts resulting from damage. Future applications of ultrahigh-resolution capabilities are illustrated with respect to direct imaging of the anisotropic potentials present in covalently bonded materials.

**(Keywords: HREM; experimental imaging, structure–image relationship)**

## INTRODUCTION

High-resolution electron microscopy (HREM) corresponds to imaging with electrons by phase contrast at a resolution sufficient to resolve the local packing of atoms and molecules into a crystalline lattice. At this resolution (nominally less than 2 nm), the image intensity is related to the projected electron potential of the sample. Because spacings corresponding to the crystalline lattice are a common feature in HREM images, these micrographs are often described as 'lattice images'.

Although HREM investigations of inorganic materials are now common, the use of this technique for organic materials (like most polymers) has been limited by the rapid degradation of the material in the electron beam. However, the careful use of minimum-dose exposure techniques as well as particular attention to sample preparation have now made it possible to apply HREM to a number of polymer systems.

Although HREM imaging is a powerful tool for structural characterization, it is imperative that the relationship between sample structure and image contrast be well understood. Certain features of HREM images correspond not to the sample but to the operating characteristics of the instrument itself. Recognizing the origins of these effects is necessary to avoid improper interpretation of the information. As with any technique, it is important that conclusions drawn from HREM experiments be tested by theoretical simulations and whenever possible corroborated by complementary approaches.

In this article the details of HREM imaging of polymers will be reviewed. In particular, the relationship between the intensity distribution in a HREM image and the original sample structure will be examined. While the relative intensities of different frequencies originally present in the sample may be altered in the image, the periodicities or 'spacings' are not changed. Hence, it is possible to associate regions of well defined periodic lattice fringes observed in HREM images as arising from similar well ordered regions present in the original sample.

We will explore these points in more detail by examining the theoretical relationship between polymer sample structure and HREM images. These image simulations use the multislice approach to solve the dynamic electron scattering from projections of the polymer crystal structure. The simulations illustrate the relationship between the postulated sample structure and the expected HREM image. Next, the history of HREM imaging of polymers and some highlights of these previous studies will be discussed. Then, experimental details pertinent to HREM studies will be presented, including sample preparation, instrument operation and sample thickness determinations. We will also examine the obscuring effect of limited electron dose and sample drift on simulated images. Finally, we address the

* Presented at 'Aspects of Imaging in Polymer Science', 51st Annual Meeting of the Microscopy Society of America, 1–6 August 1993, Cincinnati, OH, USA

† To whom correspondence should be addressed

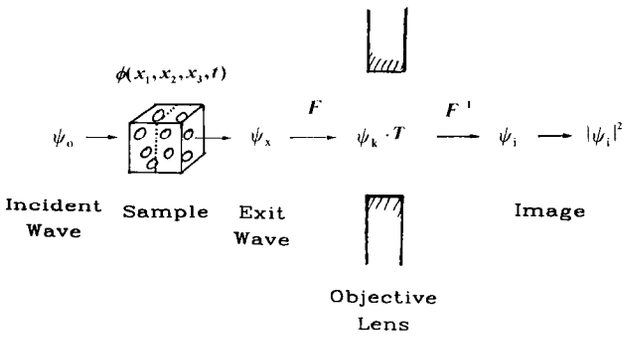


**Figure 1** Schematic of the HREM imaging process. The wavefunction of the sample is represented by $\phi$. Impinging upon the sample is an electron beam with its own characteristic wavefunction $\psi_0$. The beam interacts with the sample to give rise to an exit wave $\psi_x$. The Fourier transform of $\psi_x$ is $\psi_k$, where $k$ is the scattering vector. The effect of the objective lens is to multiply $\psi_k$ by a contrast transfer function $T$, and then to inverse Fourier transform $\psi_k T$ to give $\psi_i$, the image wave. The intensity of the final image is recorded as a two-dimensional array of darkening on the photographic film $I(x_1, x_2)$, which is proportional to the squared amplitude of $\psi_i$

implications of continued improvements in resolution on future work in this field. In particular, we discuss the developments in instrumental capability that would be necessary to resolve anisotropies in the distribution of electrons around a carbon atom due to molecular-orbital hybridization.

## THEORY: THE PHYSICS OF IMAGING AND SIMULATION

### *HREM details*

HREM has become an important tool for structural studies in materials science. Detailed reviews of the procedure are now available[1–4]. The use of HREM to reveal information about organic crystal structures has been described by Kobayashi and Isoda[5]. The possibilities of using HREM for studying defects in crystalline polymers have been discussed by Martin and Thomas[6], Tsuji[7], Voigt-Martin *et al.*[8] and Martin *et al.*[9]. The following is a condensation of the essentials of HREM imaging necessary to understand the manner in which the microscope influences the contrast in the final image. Special emphasis is given here to topics of particular interest for low-dose imaging.

*Figure 1* is a schematic of the HREM imaging process. We take the electron potential function of our sample as $\phi(x_1, x_2, x_3, t)$, where $x_1$, $x_2$, $x_3$ are positions in real space and $t$ is time. The electron beam may cause changes to the sample structure $\phi$ as a function of $t$. Images are obtained by exposing metal halide film, a YAG (yttrium aluminium garnet) crystal, or CCD (charge-coupled device) camera to the beam. This involves an integration over some time interval. We therefore restrict our discussion of the imaging process to a time-invariant structure $\phi(x_1, x_2, x_3)$.

Impinging upon the sample is an electron beam with its own characteristic wavefunction $\psi_0$ travelling in the direction $x_3$. The beam interacts with the sample to give rise to an exit wave $\psi_x$. The Fourier transform of $\psi_x$ is $\psi_k$, where $k$ is the scattering vector. With the microscope objective lens off, the experimentally observed quantity is the scattering pattern $I(k)$, which is proportional to the squared amplitude of $\psi_k$. The effect of the objective lens is to multiply $\psi_k$ by a contrast transfer function (CTF) $T$ (which depends sensitively on the operating conditions of the microscope), and then to inverse Fourier transform $\psi_k T$ to give $\psi_i$, the image wave. The intensity of the final image is recorded as a two-dimensional (2D) array of darkening on the photographic film, $I(x_1, x_2)$, which is proportional to the squared amplitude of $\psi_i$.

The goal of HREM imaging is to relate the 2D image intensity $I(x_1, x_2)$ to the 3D sample structure $\phi(x_1, x_2, x_3)$. In order to reconstruct $\phi(x_1, x_2, x_3)$ from $I(x_1, x_2)$, three problems must be solved. First, it is necessary to determine how the structure scatters the incident wave $\psi_0$ to give rise to an exit wave $\psi_x$. Secondly, it is necessary to know the effect of the microscope on taking this exit wave and producing an image wave $\psi_i$. This requires an understanding of the transfer function $T$. Thirdly, since the sample structure is 3D and the image is 2D, it is necessary to reconstruct the 3D structure by taking a series of images about some tilt axis[10].

### *Interaction of incident wave with sample*

In general, the scattering from an arbitrary arrangement of atoms requires the solution of the 3D Schrödinger equation for the entire sample–incident wave system. However, in certain limiting cases the relationship between the sample structure and the exit wave is simply related.

The effect of the positive potential distribution $\phi$ of the sample on an incident plane wave $\psi_0$ is to cause an acceleration of the electron, causing a small reduction in wavelength. This gives rise to a local phase shift for an electron passing through an area of the sample of higher potential. The amount of phase shift relative to vacuum for an electron passing through a region of uniform potential $\phi$ of thickness $t$ is $\sigma\varphi t$, where $\sigma$ is given by $\sigma = \pi/\lambda V_0 = 2\pi me\lambda/h$; $\lambda$ is the wavelength of the electron, $V_0$ the accelerating voltage, $m$ the electron mass and $e$ the electronic charge.

For high accelerating voltages, the wavelength of the electron calculated from the de Broglie relationship must be corrected for relativistic effects. The algebraic relationship between $\lambda$ (nm) and $V_0$ (volts) is[11]:

$$\lambda = 1.22639/(V_0 + 0.97845 \times 10^{-6} V_0^2)^{1/2} \quad (1)$$

Hence, for an accelerating voltage $V_0$ of 200 kV, the wavelength of the electron $\lambda$ will be 2.51 pm, and therefore $\sigma$ will equal $6.26\,\text{nm}^{-1}\,\text{V}^{-1}$. This means that a typical sample of thickness $t$ of 10 nm with a constant inner potential $\phi$ of 10 eV would cause a phase shift of 0.626 rad (35.8°) relative to vacuum.

For a thickness over which focus variation is negligible, the sample acts as a pure phase object, and the exit wave $\psi_x$ is related to the incident wave $\psi_0$ as follows:

$$\psi_x = \psi_0 \exp[-i\sigma\phi(x_1, x_2)] \quad (2)$$

where $\phi(x_1, x_2)$ (V nm) is the total projection of $\phi$ along the beam direction $x_3$, given simply by integrating $\phi$ in the $x_3$ direction. This is known as the strong phase object approximation (SPOA). The SPOA represents the correct dynamical solution to the scattering problem when the voltage is infinite[12].

If the amount of phase shift is small, the exponential in (2) may be expanded and higher-order terms neglected,

giving:

$$\psi_x = \psi_0[1 - i\sigma\phi(x_1, x_2)] \quad (3)$$

which is the weak phase object approximation (WPOA). In the WPOA case there is a simple, linear relationship between the projected potential of the sample and the exit wave. For samples of higher atomic weight, significant dynamical (multiple scattering) effects are seen in thicknesses as small as 1 nm[13]. For lower-atomic-number samples, $\phi(x_1, x_2)$ is smaller, so that the WPOA holds for thicker samples.

The solution of the dynamical scattering problem for a thick sample can be calculated by the 'multislice' method of Cowley and Moodie[14]. In this approach the sample is treated as a series of $N$ thin slices along the beam direction. The slice thicknesses are chosen so that the defocus variation within each of them is negligible, and therefore the SPOA holds. The smearing of the wave through the vacuum between slices is treated by a spherical Fresnel propagator. In the limit of large $N$, the results obtained by this technique are equivalent to the rigorous dynamical scattering calculation[14]. The multislice approach can be easily adapted for numerical calculations, and FORTRAN source code is distributed by the National Centers for High Resolution Electron Microscopy at Arizona State University and the Lawrence Berkeley Laboratory. Commercially available packages including MacTempas (Lawrence Berkeley Laboratory) and Cerius (Molecular Simulations Inc.) are also available for this purpose.

*Physics of image formation*

If the exit wave is allowed to propagate in a uniform potential field, then at large distances away from the sample the resulting wave is $\psi_k$, the scattered wave; $\psi_k$ is the Fourier transform of $\psi_x$. Without the action of the objective lens the squared amplitude of $\psi_k$ may be collected on film as the electron diffraction pattern.

The effect of the objective lens of the microscope on the propagating wave can be represented as the multiplication of $\psi_k$ by a function $T$ (known as the contrast transfer function (CTF) of the instrument) followed by the inverse Fourier transformation of $\psi_k T$ to give the image wave $\psi_i$. Ideally, it would be best to have a transfer function $T = 1$ for all frequencies; then the intensity in the image could be directly related to intensities in the exit wave. However, $T$ is a sensitive function of the optics of the microscope, and in fact may even be zero or negative. Thus some frequencies may be lost completely or passed in reverse contrast. $T$ approaches zero for low frequencies, is nearly equal to $+1$ or $-1$ for a 'pass band' of intermediate frequencies (which depend sensitively on defocus), oscillates strongly at higher frequencies, and then approaches zero again at the very highest frequencies.

The functional form of $T$ is[15]:

$$T = \exp[i\chi(k, \Delta f)]D_1(k)D_2(k, \Delta f)D_3(k, M)A_1(k) \quad (4)$$

where $\Delta f$ is defocus, $M$ is magnification, $\exp[i\chi(k)]$ is the objective lens propagator function, $D_1$ is the damping envelope due to focus spread, $D_2$ is the damping due to beam divergence, $D_3$ is the damping due to the detector response and $A_1$ is an aperture function.

The first term in equation (4) is the objective lens propagator function $\exp[i\chi(k)]$, which plays a critical role in determining the phase contrast of a high-resolution electron micrograph. The specific form of $\chi(k)$ *is*:

$$\chi(k) = 2(\pi/\lambda)(\Delta f k^2\lambda^2/2 + C_s\lambda k^4/4) \quad (5)$$

where $C_s$ is the spherical aberration coefficient of the objective lens. For a JEOL 2000 FX with a side-entry goniometer and high-resolution pole piece, $C_s = 2.3$ mm. Negative values of $\Delta f$ mean an underfocused objective lens. The term $\exp[i\chi(k)]$ is sometimes called the coherent phase-contrast transfer function[15] because it represents the expected objective lens phase shifts for a perfectly coherent source. In reality, electron sources are not coherent; their finite chromatic aberration and beam divergence both serve to dampen high-resolution information. Before we discuss the role of the function $\exp[i\chi(k)]$, we will first discuss these damping functions.

The damping function $D_1$ is due to focal spread and is given as:

$$D_1 = \exp(-\pi^2\sigma_d^2 U^4/2) \quad (6)$$

where $\sigma_d$ is the dimensionless spread of focus given in reduced units as $\sigma_d = \sigma'_d/(C_s\lambda)^{1/2}$, with $\sigma'_d$ the standard deviation of focus in nanometres. Here, $U$ is a reduced scattering vector $U = k(C_s\lambda^3)^{1/4}$. Likewise, $D_2$ is given by:

$$D_2 = \exp[-\pi^2\theta^2 U^2(U^2 + \Delta f')] \quad (7)$$

with $\theta = a(C_s/\lambda)^{1/4}$ the reduced semi-angular divergence for the beam divergence $a$ in radians, and $\Delta f' = \Delta f/(C_s\lambda)^{1/2}$ the reduced defocus.

The film damping term $D_3$ is described well by a Lorentzian[16]:

$$D_3 = 1/1(1 + Ak^2/M^2) \quad (8)$$

where $A$ is a constant, which depends on the grain size of the film and developing conditions, and $M$ is the magnification. This damping term represents the inability of the film to record incident periodic signals with very small spacings between peaks (high frequencies). The response of a photographic emulsion as a function of signal frequency is called the modulation transfer function (MTF)[17,18]. For beam-resistant samples the magnification $M$ can be increased to a point where the effect of $D_3$ on the recorded image is negligible ($D_3 = 1$). This is not the case with beam-sensitive materials, where low magnifications are important to reduce the incident electron dose. At low magnifications $D_3$ becomes the dominant damping term.

Each of the functions $D_1$, $D_2$ and $D_3$ damp high frequencies and therefore each may determine the practical limit for information transfer in the microscope. In order to evaluate the different damping functions $D_1$, $D_2$ and $D_3$, it is necesssary to define some level of intensity necessary for frequencies to make an important contribution to the image. A convenient value[15] is 14%, representing $\exp(-2)$. This level of the image intensity gives $\exp(-1)$ in the image amplitude (37%). Let us define the maximum resolution (largest important scattering vector $k$) as $k_{max}$. From equation (6), we then find the relation:

$$\sigma'_d = 0.45/(k_{max}^2\lambda) \quad (9)$$

Likewise, from equation (7) we obtain the requirement:

$$a < 0.32/[k_{max}(k_{max}^2 C_s\lambda^2 + \Delta f)] \quad (10)$$

as the limiting value of beam divergence necessary to

**Table 1** HREM imaging parameters for a JEOL 2000 FX with side-entry goniometer and high-resolution pole piece

| Parameter | Symbol | Value | Units |
|---|---|---|---|
| Voltage | $E_0$ | 200 | kV |
| Wavelength | $L$ | 0.00251 | nm |
| Spherical aberration | $C_s$ | 2.3 | mm |
| Defocus spread | $\sigma'_d$ | 5.0 | nm |
| Beam divergence | $a$ | 0.1 | mrad |
| Film damping | $A$ | $1.2 \times 10^9$ | $nm^2$ |

avoid damping due to $D_2$. Experimentally, it has been found that, with a JEOL 2000 FX, it is possible to image the 0.17 nm (840) reflection in poly(*p*-xylylene) (PPX)[19], corresponding to a $k_{max}$ of 5.88 $nm^{-1}$. From the equations above and the physical characteristics of the microscope ($C_s = 2.3$ mm, $\lambda = 2.51$ nm), this corresponds to a maximum defocus spread $\sigma'_d$ of 5.2 nm and a limiting semi-angle of illumination $a$ of about 0.1 mrad.

Experimentally, the parameter $A$ in $D_3$ may be determined by measuring the response of the film to a beam-stable object of known periodicity. This involves taking a series of lattice images as a function of magnification and determining the smallest magnification at which it is still possible to detect Fourier peaks of the appropriate frequency in the digital or optical transform of the image. On a JEOL 2000 FX, it was found that a 1.4 nm lattice image of an oxide sample could not be resolved below 10 000 × on Kodak SO-163 Electron Image Film developed in full-strength D-19 developer for 12 min. This corresponds to a peak-to-peak distance on the film of 14 $\mu$m. Using a value of $D_3$ equal to 0.14 as the limit of reasonable detection, this gives a value for $A$ of $1.2 \times 10^9$ $nm^2$. For a HREM micrograph of a 0.55 nm lattice (corresponding to the poly(*p*-phenylene benzobisoxazole) (PBZO) (200) first equatorial spacing) taken at 130 000 ×, the film damping term $D_3 = 0.81$. *Table 1* summarizes the experimental parameters governing HREM imaging with a JEOL 2000 FX and Kodak SO-163 film.

Let us now examine the expected HREM image intensity in the case of the WPOA[15]. In the following discussion the role of the damping functions $D_1$, $D_2$ and $D_3$ will be assumed unimportant. The WPOA gives us the normalized transmission function $q(x_1, x_2)$:

$$q(x_1, x_2) = \psi_x/\psi_0 = 1 - \sigma\phi(x_1, x_2) \tag{11}$$

The image plane wave is then given by:

$$\psi_i = q(x_1, x_2) * tf(x_1, x_2) \tag{12}$$

where $*$ is the convolution operator and $tf(x_1, x_2)$ is the Fourier transform of $\exp[i\chi(k)]$. The transform $tf(x_1, x_2)$ is a complex function, which can be written in terms of its real and imaginary parts $s(x_1, x_2) + ic(x_1, x_2)$. The intensity at the image plane is then:

$$I(x_1, x_2) = [1 + \sigma\phi(x_1, x_2) * s(x_1, x_2) - i\sigma\phi(x_1, x_2)c(x_1, x_2)] \times [1 + \sigma\phi(x_1, x_2) * s(x_1, x_2) + i\sigma\phi(x_1, x_2)c(x_1, x_2)] \tag{13}$$

Dropping terms of second order in $\sigma\phi(x_1, x_2)$ gives:

$$I(x_1, x_2) = 1 + 2\sigma\phi(x_1, x_2) * s(x_1, x_2) \tag{14}$$

The exponential $\exp[-i\chi(k)]$ may be written as $\cos[\chi(k)] - i\sin[\chi(k)]$, and therefore $s(x_1, x_2)$ is the Fourier transform of $\sin[\chi(k)]$.

The function $\sin[\chi(k)]$ modulates the amplitude of the scattered frequencies for weak phase objects. For optimum imaging, it would be ideal to have $\sin[\chi(k)] = +1$ or $-1$ for all important frequencies $k$. However, examination of equation (5) shows that in general $\sin[\chi(k)]$ may vary widely and is a sensitive function of the operating conditions ($C_s$ and $\Delta f$).

The immediate implication of this result is that the contrast in HREM images depends on the size of the object being examined. The phase contrast tends towards zero as the scattering vector $k$ decreases (i.e. the size of the object increases). When $k$ is small, the second term in $\sin[\chi(k)]$ (with $k^4$ dependence) will be much smaller than the first. In this case the optimum focus for imaging a feature of size $d = 1/k$ by phase contrast is approximately $\Delta f = -d^2/2\lambda$. This expression is valid for features with a spacing of $d \gtrsim 0.6$ nm. For example, the appropriate amount of defocus necessary to image a lattice spacing of $d = 1.25$ nm with $\lambda = 2.51$ pm is $\Delta f = -311$ nm.

At a slight underfocus of the objective lens, there are focus conditions where $\sin[\chi(k)]$ is nearly equal to $-1$ over a broad range of frequencies. This focus setting is called the Scherzer focus, after Otto Scherzer, who was the first to describe it[20]. The Scherzer focus is given by $\Delta f = -(C_s\lambda)^{1/2}$. Examination of the function $\sin[\chi(k)]$ reveals that there are a range of objective lens focus settings near Scherzer that will give generally useful high-resolution imaging conditions. An alternative setting of the objective lens is the 'extended' Scherzer focus at $\Delta f = -(\frac{3}{2}C_s\lambda)^{1/2}$. At the extended Scherzer focus the first zero in the transfer function occurs slightly further out in reciprocal space at the expense of a small fluctuation in the value of $\sin[\chi(k)]$ at intermediate values of $k$. The reciprocal of the first zero in the transfer function ($1/k_s = d_s$) is a measure of the optimum resolution of the microscope. At the extended Scherzer focus condition, the resolution is:

$$d_s = 0.66(C_s\lambda^3)^{1/4} \tag{15}$$

From this expression it is evident that the resolution of a microscope is determined by the value of the spherical aberration coefficient ($C_s$) and the wavelength ($\lambda$), which is in turn a function of the operating voltage ($V_0$). Since the wavelength is inversely related to voltage (equation (1)), improvements in resolution require increasing $V_0$ and decreasing $C_s$. The theoretical resolution $d_s$ is shown in *Figure 2* as a function of $C_s$ and $V_0$. Also plotted on the diagram are the operating characteristics of several current-generation instruments used for HREM. For a JEOL 2000 FX the Scherzer focus is $-76$ nm and the theoretical resolution $1/k_s = d_s = 0.29$ nm.

For an ideal objective lens, $\chi(k) = -\pi/2$ for all frequencies, giving $\sin[\chi(k)] = -1$ for all $k$. In this optimal case, equation (14) becomes:

$$I(x_1, x_2) = 1 - 2\sigma\phi(x_1, x_2) \tag{16}$$

Equation (16) shows that for a sample obeying the WPOA imaged in an ideal lens, the HREM image intensity distribution will be linearly related to the projected specimen structure $\phi(x_1, x_2)$. Equation (16) also indicates that atoms (high potential) will appear darker (less intensity) then neighbouring vacuum ($\phi = 0$). Under these stringent experimental conditions, HREM image inter-

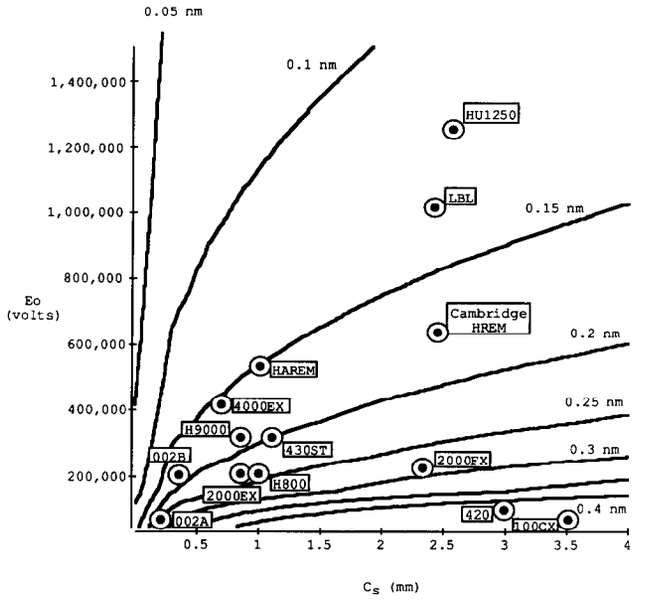


**Figure 2** Theoretical resolution as a function of operating voltage. Increasing the resolution requires increasing the voltage and decreasing the spherical aberration coefficient of the objective lens. The capabilities of current-generation instruments are indicated

pretation is intuitive. For other defocus settings, dark areas are not necessarily a direct mapping of regions in the sample with a high projected potential. The maximum amount of contrast in the image under optimum conditions is given by $2\sigma\phi_{max}(x_1, x_2)$.

Note that in a real image the amount of contrast will never be this high; oscillations in $\sin[\chi(k)]$ and the damping functions $D_1$, $D_2$ and $D_3$ will all dampen the intensity of different frequencies in an actual experimental image. However, the equation represents a lower bound for the minimum $\phi(x_1, x_2)$ necessary to give the observed contrast in a micrograph. Hence, by measuring the experimentally obtained HREM image contrast, one can estimate the minimum amount of local variations in $\phi$ in the sample. Quantitative measurements such as these are of interest for detailed comparison of structural models with experimental images, particularly for highly disordered systems where models might predict a smaller amount of variation in $\phi$ than could be explained by the observed HREM contrast.

The actual contrast for a known sample and microscope configuration can be calculated if the full dynamic scattering of the material is known. As mentioned earlier, a convenient method of calculating the dynamic scattering problem is the multislice formalism.

*Image simulations: multislice*

If the dynamic scattering of a crystal structure of a given thickness is known, then it is possible to calculate experimental HREM images if the operating parameters of the microscope are also known. A comparison of calculated images with those experimentally obtained is further support for the validity of a given structural model. Such comparisons are now routinely performed in HREM studies of inorganic materials.

Multislice image calculations make it possible to anticipate what should be expected in the HREM study of a new sample. They can be used to develop more detailed models to account for local variations in microstructure from experimental images. However, because of the computationally intensive nature of these calculations and the large number of parameters involved, caution must be employed in the detailed interpretation of simulation results. For example, in a study of oxygen ordering in superconductors, Ourmazd and Spence used image calculations to suggest that certain white rows seen in HREM images could be interpreted in terms of different types of ordering on the oxygen-deficient planes[21]. However, Huxford *et al.* showed with similar calculations that variations in Debye–Waller factors could also lead to image predictions similar to those seen with vacancy ordering[22].

There are other deficiencies in the multislice calculation that may lead to errors and therefore deserve mention. Most of the multislice programs in use rely on the Mott formula for approximating the electron scattering factor[23]. Peng and Cowley have shown that the Mott formula can lead to serious errors in simulated images and potential distributions, particularly for large objects (small frequencies)[24]. This is not a problem for small unit cells, but becomes critical for simulations of large objects and for extended cells containing defects. Also, the scattering factors that are incorporated are all assumed to be spherically symmetric about the atomic centre. The deviations from local symmetry that arise from hybridization of the electrons into molecular orbitals have not yet been incorporated into the multislice approach. These effects might be particularly significant in low-atomic-number materials with strong molecular-orbital hybridization and aromaticity.

Another limitation in current formulations of the multislice approach is in determining image contrast for small deviations off the Bragg angle. Such predictions are important for understanding the 'rocking curve' behaviour of HREM images. As currently written, multislice packages recalculate a 2D unit cell that describes the periodic projection of the structure in a given crystallographic direction. For small deviations from a Bragg reflection, the projection may be along a non-crystallographic direction. In such a case, the program calculates a slice thickness that is prohibitively large (often over 100 nm). This method of creating 'periodic slices' also limits the ability to determine easily the effect of thin sections through samples with large unit cells.

*Simulated HREM images of rigid-rod polymers*

Poly(*p*-phenylene benzobisthiazole) (PBZT) and poly(*p*-phenylene benzobisoxazole) (PBZO) are rigid-rod polymers that have been examined for lightweight, high-modulus, high-strength fibres. The microstructures of these polymers have been studied by HREM in some detail[25–27]. Here, we examine simulated images of these materials to explore the relationship between the projected electron potential and the experimental image. The coordinates of the atoms used in these calculations were determined by Adams and Fratini[28]. For PBZO, the unit cell used was monoclinic and non-primitive, with $a = 1.1039$ nm, $b = 0.3458$ nm, $c = 1.2061$ nm, $\alpha = 90°$, $\beta = 90°$ and $\gamma = 91.50°$. The position of the second PBZO chain was chosen to be (1/2, 0, 1/4), in order to be consistent with experimental wide-angle X-ray scattering (WAXS) and selected-area electron diffraction (SAED) data[27].

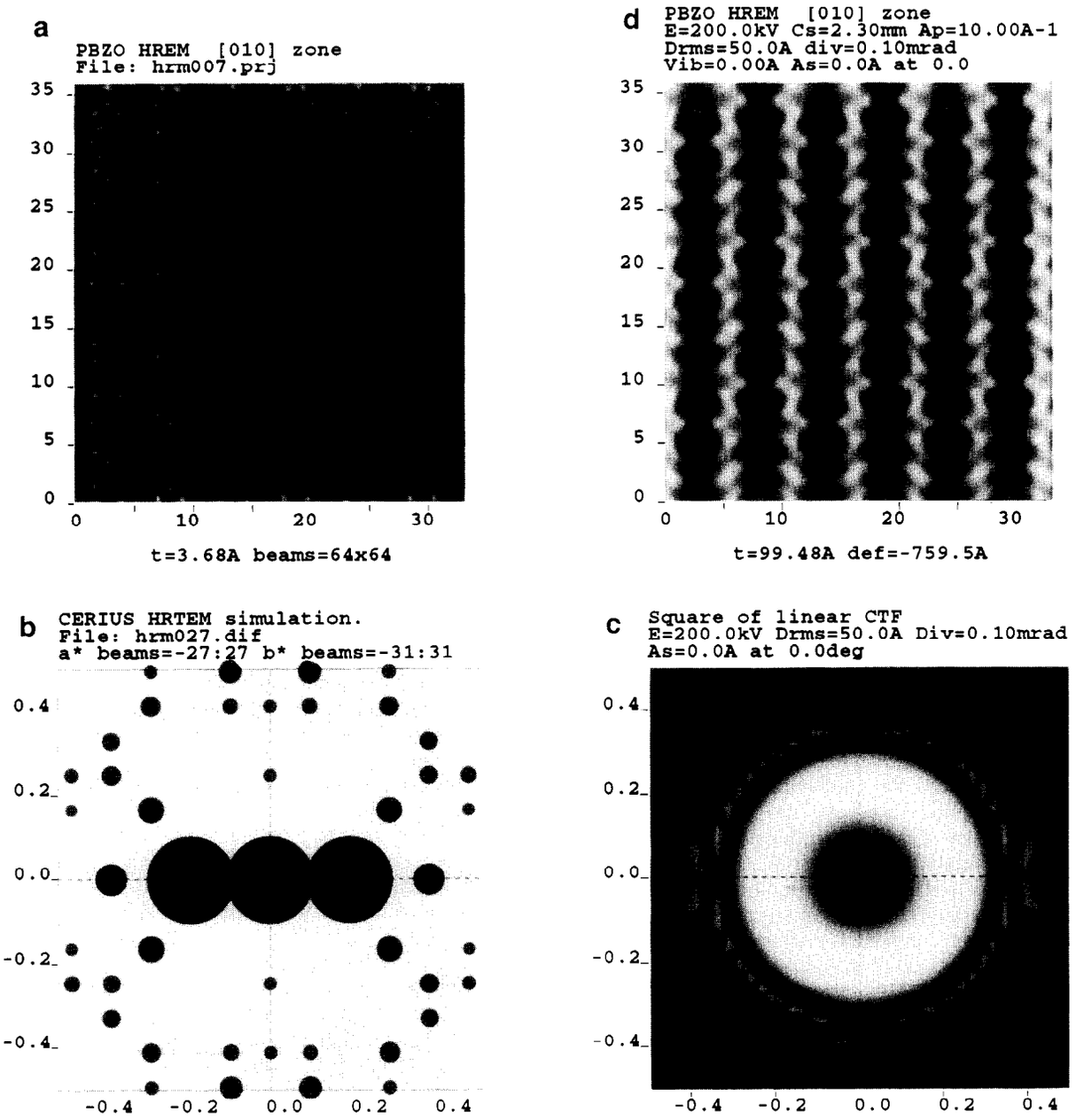


**Figure 3** (a) Projected potential of PBZO in the [010] direction. The molecules associate laterally at a characteristic spacing of 0.55 nm. (b) Dynamic electron diffraction pattern for a 10 nm slice of PBZO in the [010] direction. The intensities of the Bragg reflections are represented by the diameters of the spots. The 0.55 nm (200) reflections are predicted to be the most intense, as observed in experiment. (c) Amplitude of the contrast transfer function for a 200 kV JEOL 2000 FX at Scherzer focus. (d) Simulated HREM image of a 10 nm slice of PBZO projected in the [010] direction at Scherzer focus. Comparison with (a) reveals that, while the high-resolution details about the hydrogen atoms and internal structure of the phenyl and heterocyclic group cannot be resolved, it is possible to determine the positions of the stacks of polymer chains. At Scherzer focus, the stacks of molecules are in reverse contrast, with the image predicted to be dark where the projected potential is high, and light where the projected potential is low

In PBZO the planes of highest electron density are the 0.55 nm (200) and 0.35 nm (010) planes parallel to the chain axis. These planes correspond to lateral close packing between molecules 'side-to-side' and 'face-to-face' respectively. Similar spacings are also observed in PBZT. *Figure 3a* shows the projected electron potential of PBZO in the [010] direction. The general shape of the PBZO molecules can be easily distinguished.

*Figure 4a* shows an electron diffraction pattern from a thin section of PBZT fibre. On the same scale in *Figure 4b* is shown the square of the function $\sin[\chi(k)]$ at Scherzer focus. *Figure 4c* shows the product of *Figures 4a* and *4b*. Note that the first zero in $\sin^2[\chi(k)]$ occurs just after the second equatorial reflection. Also, the third-order layer line is the last meridional reflection within the band-pass zone.

For comparison, *Figures 4d* and *4e* show the corresponding amplitude of the CTF at Scherzer focus for a microscope with $C_s = 0.7$ mm and $\lambda = 1.64$ pm, corresponding to values for a JEOL 4000 FX microscope

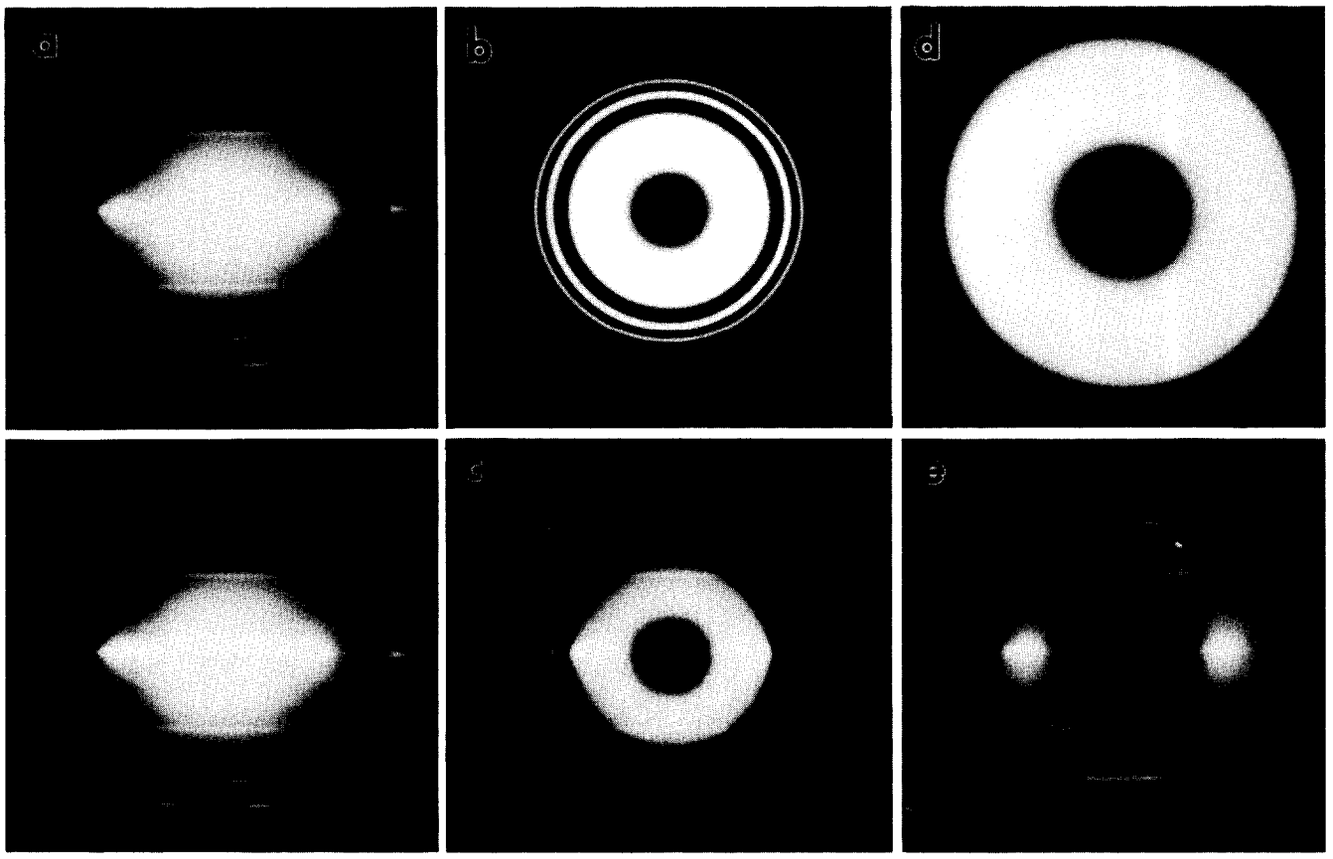

**Figure 4** (a) Electron diffraction pattern from a thin section of PBZT fibre. (b) Square of the function $\sin[\chi(k)]$ at Scherzer focus. (c) Product of (a) and (b). Note that the first zero in $\sin^2[\chi(k)]$ occurs just after the second equatorial reflection. The theoretical resolution of this instrument is 0.29 nm. (d) Square of the function $\sin[\chi(k)]$ at Scherzer focus for a microscope with $C_s = 0.7$ mm and $\lambda = 1.64$ pm, corresponding to values for a JEOL 4000 FX microscope operating at 400 kV. (e) Product of (a) and (d). Here, the first zero occurs at a frequency corresponding to a resolution of 0.16 nm, because of the higher operating voltage and lower $C_s$

operating at 400 kV. Here, the first zero occurs at a frequency corresponding to a resolution of 0.16 nm, because of the higher operating voltage and lower $C_s$.

The simulated electron diffraction pattern (*Figure 3b*), 2D contrast transfer function (*Figure 3c*) and simulated HREM images of PBZO at Scherzer focus (*Figure 3d*) were calculated using the multislice formalism with instrumental parameters characteristic of a JEOL 2000 FX (*Table 1*). The sample thickness was assumed to be 10 nm. The simulated image shows that the details of the PBZO molecules, such as the position of the hydrogen atoms and the shape of the phenyl and heterocyclic group, cannot be resolved by HREM with a JEOL 2000 FX. Nevertheless, the simulations confirm that, if there is a region of the sample that exhibits crystalline order and is oriented such that densely packed planes are parallel to the electron beam, the HREM image of this region will show a periodic modulation in intensity at a frequency corresponding to the structural modulation within the sample. For PBZO near the Scherzer focus, the strong 0.55 nm fringes are predicted to be in reverse contrast. In the simulated image there are dark bands where the projected potential is highest (under stacks of PBZO molecules).

In summary, image simulations of PBZO show that, while it is not possible to obtain information about the internal details of the polymer molecules, it is possible to image the regular packing between these molecules. Equatorial fringes with spacings of approximately 0.55 nm and 0.35 nm show regions of good lateral packing, and therefore serve to characterize precisely the local molecular orientation. Images of the meridional fringes (1.2 nm in PBZO) are sensitive to the axial registry between neighbouring chains. The extent, perfection and contrast of the lattice fringes reveal detailed information about local molecular organization.

These theoretical images were simulated using an infinite incident beam dose. In the HREM of beam-sensitive materials the dose required to form the image is an important additional experimental constraint. The effect of limited dose is to cause a local fluctuation in the experimentally observed intensity. The effect of limited dose on images can be assessed by electron counting statistics. The parameter indicative of the expected image quality of an object of size $d$ is $Q$, the number of electrons incident in an area of $d^2$. The value of $Q$ is determined simply from $J$, the total electron dose, and $d$, the size of the object, by:

$$Q = Jd^2 \tag{17}$$

This relation emphasizes that for uniform incident radiation the quality of the data (determined by $Q$) will be dependent on the size of the object of interest $d$. For beam-sensitive materials, there is a limiting amount of

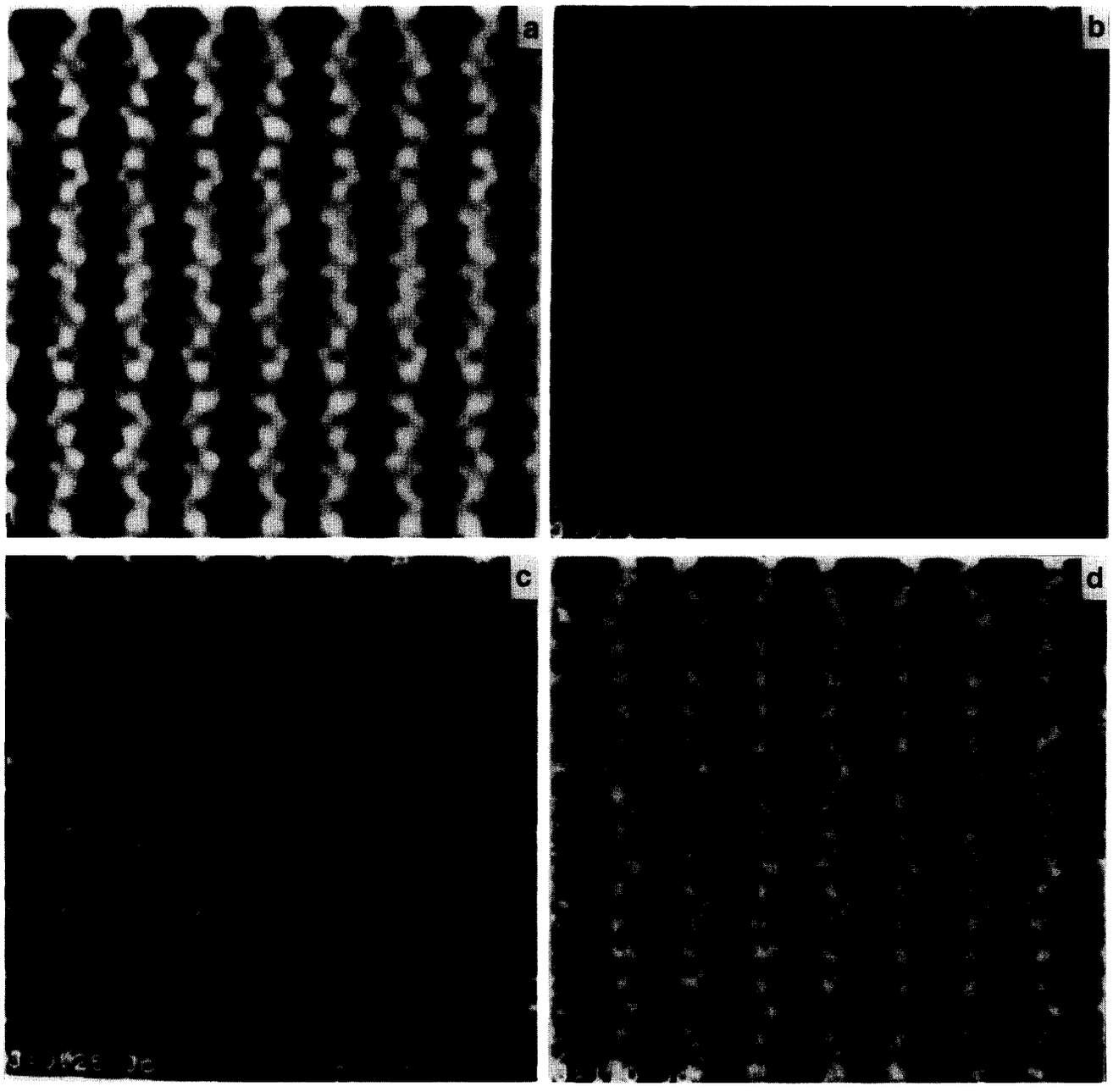


**Figure 5** Effect of limited electron dose on HREM images of PBZO. As the amount of dose increases, the statistics improve and the apparent 'noisiness' decreases. The number of electrons that pass through a given area of the sample provides a useful measure for assessing the image quality of a dose-limited object. Images at 200 kV are shown for (b) $J = 0.1J_e$, (c) $J = 0.25J_e$ and (d) $J = J_e$

radiation that the sample can withstand called the total end-point dose (*TEPD*) $J_e$. The best expected image quality for an object of size $d_1$ in a material with $TEPD = J_e$ is given by $Q = J_e d_1^2$. The standard deviation in the intensity of an object illuminated with $Q$ electrons is given by $Q^{1/2}$; hence the relative error $e$ associated with incident electron statistics of $Q$ is given by:

$$e = Q^{1/2}/Q = Q^{-1/2} \tag{18}$$

For PBZT at 200 kV, $J_e = 2.3\,C\,cm^{-2}$ ($144\,000\,e^-\,nm^{-2}$) and $d_{100} = 0.59$ nm. This gives the best estimate of $Q = 50\,000$, corresponding to an error $e$ of 0.4%. For polyethylene (PE) at 200 kV, $J_e = 0.015\,C\,cm^{-2}$ ($900\,e^-\,nm^{-2}$) and $d_{100} = 0.41$ nm; hence the maximum value of $Q = 150$, and the expected error $e$ is 8%.

It is possible to simulate the effects of limited dose on HREM images with commercially available routines in software packages such as SEMPER[29]. These routines simulate dose-limited images by using the image as a probability map for incident electrons. Pradere and Thomas have used such an approach to investigate the predictions of limited dose on theoretical and filtered images and find results that appear very similar to experimentally obtained low-dose HREM images[30]. This supports the contention that sampling statistics play an important role in practical HREM of beam-sensitive materials.

The effect of limited dose on HREM images of PBZO is presented in *Figure 5*. Images of PBZO at 200 kV are shown for $J = 0.1J_e$, $0.25J_e$ and $1.0J_e$, where

$J_e = 0.8\,C\,cm^{-2}$ ($50\,000\,e^-\,nm^{-2}$). Since the primary spacing in this image is $d_{200} = 0.55$ nm, these images correspond to $Q = 1500$, 3750 and 15000, with relative errors of $e = 2.3\%$, 1.6% and 0.8%. It is apparent that, while the positions of the fringe maxima can be interpreted with confidence, the detailed nature of local intensity variation is lost, particularly at the lowest doses. In practice, it is necessary to restrict images to doses of no more than $J_e/3$ in order to avoid using electrons scattered from partially damaged crystals.

## EXPERIMENTAL HREM OF POLYMERS: BACKGROUND

### *History of polymer HREM*

The first published image with lattice resolution of a polymer was a two-beam dark-field (DF) image of the 1.8 nm (100) spacing in beta-PPX by Bassett and Keller in 1968[31]. Although the image was noisy and the contrast low, the 1.8 nm spacings can be clearly seen over an area approximately $25 \times 75\,nm^2$. The lattice was straight and apparently free of defects over the area imaged, although the quality and limited extent of the image make a detailed interpretation difficult.

In 1975 the 0.64 nm (002) meridional and 0.43 nm (110) equatorial reflections of poly(*p*-phenylene terephthalamide) (PPTA) fibre spun from liquid-crystalline solutions were successfully imaged in bright field (BF) by Dobb *et al.*[32]. These pioneering results showed clearly the intermolecular spacings corresponding to lateral packing and intermolecular registry between PPTA molecules. The simultaneous imaging of high-contrast, straight meridional (002) fringes and (110) equatorials indicated the true three-dimensional crystallinity in this system and confirmed the extended-chain structure. Although the general features of the images were consistent with the pseudo-orthorhombic unit cell for PPTA proposed by Northolt[33], close examination of the data indicates regions where the (002) and (110) fringes coexist and make a relative angle of 85°, which conflicts with the proposed orthorhombic PPTA unit-cell angles of $\alpha = \beta = 90°$.

The size and shape of crystalline domains in PPTA as well as their relative orientation could be discerned and were compared with those determined by X-ray diffraction line-broadening studies[34]. It was noted that HREM results gave crystallite sizes that were consistent with but slightly larger than those determined by WAXS and SAED. The crystallites were small (8.6–22.5 nm) and typically free of internal defects, although some regions of more disordered lattices including curved (002) planes were seen. These results were used to rationalize the high tensile strength and relatively weak shear modulus and compressive strength of these fibres in terms of a possible delamination between the relatively weakly laterally bonded, highly oriented PPTA molecules[35].

Read and Young obtained HREM images of large plate-like crystals of solid-state polymerized polydiacetylene[36,37]. Evidence was shown for edge dislocations involving Burgers vectors perpendicular to the chain axis. Yeung and Young were able to obtain HREM images of polydiacetylenes corresponding to projections of individual polymer molecules along their chain axis[38].

A number of flexible-chain polymers have now been examined by HREM, including isotactic polystyrene (PS)[39,40], polytetrafluoroethylene (PTFE)[41] and poly(phenylene sulfide) (PPS)[42]. Single crystals[43,44] and drawn gels[45] of polyethylene (PE) have been examined. Lattice images have also been obtained in certain biopolymers including cellulose[46–49] and bacterially synthesized polyesters such as poly(hydroxybutyrate) (PHB)[50]. Polymerized sulfur nitride[51] $(SN)_x$ and poly(phthalocyaninatogermoxane)[52] crystals have also been examined by HREM.

Tsuji obtained HREM images of both the alpha (monoclinic) and beta (hexagonal) polymorphs of poly(*p*-xylylene) (PPX), and was able to visualize directly down individual chains in a flexible chain-folded single crystal[53,54]. Evidence was shown for dislocations with Burgers vectors perpendicular to the chain axis. Pradere and Thomas also studied the morphology of PPX single crystals by HREM, and used this information to develop a 3D model for twin boundaries across which the chains were parallel but the orientation of the lamellar surfaces was not[55].

Fryer *et al.* have studied low-dose HREM of crystals of several low-molar-mass organic molecules, including paraffins[56] and monolayer Langmuir–Blodgett films of phthalocyanines[57]. It has been possible to characterize the structure of grain boundaries between phthalocyanine domains and to study the high concentration of defects and misorientation in the thin monolayer films. Fryer and Dorset[58] investigated the structure of lipid systems exhibiting a lamellar texture and imaged crystal boundaries and edges as well as local fluctuations of the lamellar orientation.

Durst and Voigt-Martin[59,60] investigated the structure of main-chain and side-chain thermotropic smectic liquid-crystalline polymers by HREM. They have found defect structures including edge dislocations of different-magnitude Burgers vectors[60]. Voigt-Martin *et al.* investigated discotic liquid-crystalline polymers and have obtained projections of the ordered packing of stacks of disc-shaped mesogens[61]. A particularly interesting observation from this study was that thin films quenched from the nematic state did not exhibit the grain-boundary defects seen in crystalline films.

The PBZT lattice was first imaged by Shimamura *et al.*[25]. Evidence for the (100) lateral packing and faint, meandering (001) lines was shown. Lattice images in PBZO have been obtained by Adams *et al.*[26] and show similar evidence for good lateral ordering. Martin and Thomas obtained HREM images of PBZO as a function of heat treatment and were able to resolve the size, shape and relative orientation of the crystallites[27]. Defects within PBZO crystallites were also observed. The results were quantitatively compared with dark-field images and effective crystallite size measurements from WAXS and SAED data. Images consistent with high-angle, local bending of molecules within compressive failure zones (king bands) were obtained[62]. These observations were used to develop a classification scheme for grain-boundary defects in extended-chain polymers[63].

HREM studies of syndiotactic polystyrene (s-PS) revealed antiphase boundaries due to local variations in the crystallographic packing of the helical s-PS chains[64]. Extra reflections present in the optical diffraction patterns of the s-PS HREM images were used to reconstruct the positions of the antiphase domains via a 'dark-field' (DF) experiment on the laser optical bench.

**Figure 6** HREM image of PMDA–ODA lamellar crystals ([100] zone). The strong 1.6 nm (002) fringes correspond to the repeat distance from segment to segment along the chain backbone. The local orientation and perfection of the lamellae can be determined directly, and evidence for screw-dislocation-mediated branching is observed (arrows). Reproduced by permission from ref. 67

Masse *et al.* obtained HREM images of oriented films of the electrically active polymer poly(*p*-phenylene vinylene) (PPV)[65]. The crystallites were found to be small (4 nm), and the orientation distribution was calculated and compared to that obtained by WAXS and DF imaging. Systematic tilt studies revealed that the crystallites were randomly oriented about the orientation axis.

Martin *et al.* used HREM to examine the reorganization of polyimides during crystallization induced by imidization[66]. In particular, the influence of surface constraints was examined by monitoring microstructural evolution near the edges of thin droplets deposited on substrates. The size, shape and relative orientation of the polyimide crystallites were examined in detail. HREM images of the 1.8 nm (001) meridional spacing revealed a weak orientation of the polymer molecules parallel to the edge of the droplet. Quantitative measurements of the area fraction of the image exhibiting lattice fringes provided evidence for a strong molecular orientation in the plane of the substrate. Evidence for substantial curvature (radius of deformation $\sim 50$ nm) was observed within individual polymer crystallites, indicating large fluctuations in local molecular orientation.

Ojeda and Martin reported on HREM imaging within pyromellitic dianhydride–oxydianiline (PMDA–ODA) polyimide single crystals grown from dilute solution[67]. HREM images were obtained for zone axes both parallel and perpendicular to the chains. The strong 1.6 nm (002) fringes (*Figure 6*) provided unambiguous evidence for the local perfection of crystalline registry and order possible in PMDA–ODA crystals. Evidence for dislocation-mediated splay distortions of the lamellae were obtained. HREM images from the [001] zone revealed the 0.6 nm (100) and 0.4 nm (010) spacings. Evidence for deviations of up to 10° in the crystallographic angle $\gamma$ were observed and shown to be consistent with theoretical crystal energy calculations from molecular simulations.

Wilson and Martin used HREM to reveal evidence for crystal bending of the polydiacetylene 1,6-dicarbazolylhexadiyne (DCHD) near surfaces[68]. Small-angle grain boundaries were imaged and shown to be constructed from arrays of edge dislocations. Liao and Martin used HREM and SAED to provide information about the solid-state polymerization of DCHD by using the electron beam simultaneously to observe and induce the reaction[69]. It was found that the phase transition proceeds through a series of crystalline intermediate states. Diffraction spot broadening and streaking were also noted, indicating a certain degree of heterogeneity in the local extent of conversion.

Lieser *et al.* reported HREM images of the lyotropic liquid-crystalline polydiacetylene poly[5,7-dodecadiyne-1,12-diol-bis(n-butoxycarbonylmethylurethane)] (P4BCMU) with domains that were much larger perpendicular to the molecules than along the molecular direction[70]. This was tentatively associated with the segregation of chain ends into the featureless regions between the fringes and was used to estimate the degree of polymerization.

Hudson *et al.* obtained HREM images of the crystallization of thermotropic liquid-crystalline polymers in the smectic phase[71]. The strong (001) reflections revealed the registry between layers in the smectic phase. Crystals were observed to grow without causing a concomitant shift of the lattice fringes. This information is consistent with a mechanism of crystallization by rotations of moieties about the chain backbone.

### *Practical HREM imaging of beam-sensitive samples*

The most important constraint limiting the utility of HREM for microstructural studies of polymers is the sensitivity of organic molecules to high-energy electron beams[72]. A parameter that describes the sensitivity of a sample to the beam is the total end-point dose (*TEPD*) $J_e$, the incident electron dose required to destroy the crystalline order within the sample. The measurement of $J_e$ can be done by examining the mass loss, diffraction spot fading, or spectroscopic changes as a function of time. Most often, $J_e$ is characterized by observing the decay in intensity of sharp reflections in the SAED pattern of the originally crystalline material. A related quantity that is also used to measure beam damage is the critical end-point dose $J_c$, which is obtained by a fit of the intensity of a Bragg reflection as a function of dose to an exponential decay function:

$$I = I_d \exp(-J/J_c) + I_b \tag{19}$$

Either $J_e$ or $J_c$ is an adequate measure of the sensitivity of a sample for HREM imaging. Kumar and Adams have reported an empirical correlation between $J_c$ and the melting (or degradation) temperature $T_m$ of the polymer[73]. The experimentally determined empirical relationship

between $J_c$ ($C\,cm^{-2}$) and $T_m$ (K) can be found from the plot shown by Kumar and Adams to be:

$$\log(J_c) = T_m/150 - 5.7$$

This relationship between beam damage resistance and thermal stability was found to hold over a broad temperature range (300–1000 K).

For successful HREM of beam-sensitive materials it is important to illuminate with as few electrons as possible to avoid imaging damaged material. Also, it is useful if samples with large characteristic frequencies can be found. As shown previously, the expected image quality is determined by the local incident dose $Q = Jd^2$, where $d$ is the size of the feature of interest.

HREM studies of polymer microstructures have provided several new and important insights for solid-state polymer physics. It has been established that, as for low-molecular-weight solids, polymer crystals contain classical lattice defects such as dislocations and grain boundaries. The size, shape, relative orientation and internal perfection of certain polymer crystals have now been determined. HREM observations of rigid-rod polymers that have undergone plastic deformation in compression suggest that covalent-bond bending in rigid-rod macromolecules is possible at room temperature. The nature of crystallization in thermotropic liquid crystals has been clarified. The influence of free surfaces on the reorganization of polyimides has been elucidated, and the progress of solid-state phase transformations has been monitored.

As the quality and quantity of information of this type increase, we may expect to see further development of theoretical models to help explain these observations. With experimental images of actual defect structures in hand, it will be encouraging to explore in more detail the role such defects play in determining macroscopic properties. We also anticipate an increased effort to quantify the contrast in the image and relate this information to microstructural models.

### *HREM and dark-field imaging*

As discussed in the previous sections, HREM lattice 'fringes' are related to projections of regular molecular packing within the sample. However, it is also possible to use dark-field (DF) imaging to provide much the same sort of information by forming an image with only certain parts of the scattered radiation. In general, HREM and DF are complementary techniques and therefore should both be used to answer local microstructural questions.

One of the primary advantages of HREM is the lower electron dose necessary to form the micrograph. In DF only that part of the radiation scattered into the aperture is used to form an image. Therefore, for the same optical density from a single-crystal region on the final negative, DF will always require much more radiation. This means that DF will typically have to be performed at lower magnifications, and therefore will give poorer resolution. Accordingly, HREM is a fine-detail technique, giving information about *ultra*structure of the material at or below the molecular level. DF is more of a *micro*structure technique, and is relevant for determining crystal size and shape and general orientation, but is not as sensitive to such details as the possible disorder within these crystals or to small-angle grain boundaries between adjacent crystals.

A second advantage of HREM is that one image of a sample contains information about all of the relative orientations of crystallites in the Bragg condition simultaneously. In DF, small relative orientations cannot be easily resolved by a finite-size aperture. Likewise, it is difficult to resolve small relative variations in lattice spacing by DF. The selectivity for orientation and spacing in DF becomes better with smaller apertures, but with very small apertures high-frequency information such as detailed crystal shapes is lost. With optical bench filtering techniques it is possible to use selective apertures to reconstruct images using only certain reflections[74]. In this way, the HREM image serves as a template for subsequent analysis by 'optical DF imaging' with the laser beam.

However, HREM is certainly not without its disadvantages. In HREM imaging, there is an effective aperture function that acts to damp the response of high-frequency beams contributing to the image. Hence, it is not possible to use HREM to provide information using these higher-order reflections, since they will not be resolved in the final image. Also, because HREM images are formed with the low-angle unscattered, forward scattered and inelastically scattered electrons, there is a large d.c. level signal, which reduces the image contrast. In DF, only those beams which scatter into the aperture are used to form the image, so that the d.c. level is zero and therefore the final contrast is much higher. Another drawback of HREM is that it is time-consuming and experimentally demanding, and therefore an often unsuccessful technique. It requires careful sample preparation, microscope operation and operator patience. Also, because of the problems of beam damage, it cannot be applied with success to all systems.

## EXPERIMENTAL DETAILS

### *Sample preparation*

As in conventional TEM, HREM is most effective and reliable when examining extremely thin samples. This often poses a severe experimental constraint, for the reproducible preparation of appropriate specimens is often a challenging task.

Useful results are often obtained by depositing the sample directly onto an amorphous carbon film that has been deposited onto a freshly cleaved mica sheet[66,67]. The film can then be removed from the mica by floating onto a water bath, followed by lifting with copper TEM grids. The supporting film helps to stabilize the sample, significantly reducing drift during exposure. A particularly convenient sample geometry is provided by droplets deposited onto the surface. The edge of the droplet provides a convenient reference point at which the thickness of the sample goes to zero.

It is also possible to microtome sections that are thin enough for successful HREM. Reproducible sections can usually be obtained down to 50 nm thickness with an ultramicrotome and a good diamond knife.

Another technique used to obtain thin sections of fibrous materials is called 'detachment replication'[25,27]. This technique takes advantage of the relatively weak lateral bonding of the fibres. The fibre is embedded into a collodion substrate and the bulk of material removed, leaving thin fragments of material behind. The fragments

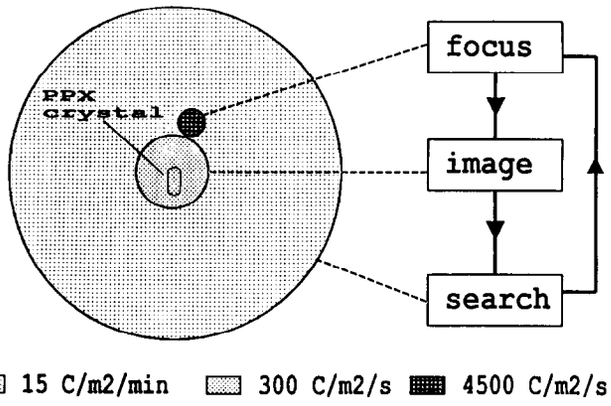


**Figure 7** Schematic of the experimental procedures used when applying the minimum-dose system (MDS) to low-dose HREM imaging of polymers. Samples are searched with a defocused (000) diffraction spot. When an area of interest is found, the beam is focused on an adjacent region of the support film before imaging

of the fibre are then suspended on a holey carbon grid by dissolving away the collodion with amyl acetate.

*Instrument operation: low-dose HREM*

An instrument with sufficient capabilities for low-dose HREM of polymers is a JEOL 2000 FX Transmission Electron Microscope operating at 200 kV. The microscope can be equipped with a high-resolution objective lens pole piece (spherical aberration coefficient $C_s = 2.3$ nm) and a minimum-dose system (MDS) that allows the operating conditions of the microscope to be changed quickly during operation. Also, a beam blanking device may be installed for manually deflecting the beam away from the sample at the condenser lens level in the column.

All HREM operation requires careful alignment and astigmation corrections[75,76]. The astigmatism of the objective lens depends critically on the exact position of the objective lens aperture[1]. In the HREM studies reported here, no objective aperture was used. Current generations of microscopes make it possible to monitor quantitatively the value of the various lens currents, significantly improving the speed and reproducibility of proper alignment procedures.

The procedure for low-dose imaging of a sample is as follows: First, the microscope is carefully aligned and stigmated using high magnification (250 000 × or more) on the grain of a carbon film using a Gatan video screen coupled to an image intensifier system. Then, the conditions appropriate for imaging are selected. Typically, film sensitivity requires that imaging be done at a screen current of 10 pA cm$^{-2}$ and an exposure time of 0.5–1.0 s. As mentioned earlier, it is important to restrict exposure at the sample to less than $J_e/3$ to avoid imaging the damaged lattice. The dose at the sample is given by:

$$J = jtM^2$$

where $j$ is the current dose rate at the viewing screen, $t$ is the exposure time and $M$ the magnification.

*Figure 7* shows a schematic of the imaging conditions used during low-dose HREM observation[77]. First, the operating conditions are prepared for the final photograph including astigmation and beam alignment (voltage centring). Typically, this involves an intermediate setting of the first condenser lens (spot size 4) with a screen current of 5 pA cm$^{-2}$ and exposure time of 1 s. This results in an average optical density of ~0.5 on Kodak SO-163 film developed for 12 min in straight D-19. For a magnification of 130 000 ×, this corresponds to a dose rate of 0.08 C cm$^{-2}$ s$^{-1}$ at the sample. Then, the MDS system is initiated, causing these lens conditions to be recorded as 'PHOTO' mode. Next, the system is switched to 'SEARCH' mode and the microscope placed in diffraction conditions. The condenser lens is adjusted to reduce the beam flux (spot size 6 of a JEOL 2000 FX), causing a large decrease in the intensity (two orders of magnitude). Defocusing the diffraction pattern provides sufficient contrast in the (000) beam for this low-magnification BF image be used to search the sample for an appropriate area for HREM imaging. The magnification of this defocused central spot image can be controlled with the diffraction focus, and it is convenient to check for proper sample thickness and orientation by focusing back to the diffraction pattern. Once a suitable place on the sample has been found, the beam was translated to an adjacent region for focusing. The microscope was then switched to 'FOCUS' mode and the 'IMAGE SHIFT' controls were used to move the beam back to the centre of the screen.

With practice and at high operating magnification (100 000–250 000 ×), it is possible to focus on an area adjacent to the sample at the same magnification as originally set in 'PHOTO' mode. This is not possible when imaging at lower magnifications, in which case it is important to calibrate any possible shift in focus that occurs after a magnification change between 'FOCUS' and 'PHOTO' modes. Scherzer focus was obtained by defocusing a known number of fine objective lens clicks from the minimum contrast, which occurs at the Gaussian focus. For a JEOL 2000 FX this corresponds to 16 steps at 4 nm/step. The position of minimum contrast[78] occurs at 0.3 Sch, where Sch is the Scherzer focus. For a JEOL 2000 FX, the Scherzer focus is −76 nm and the Gaussian focus is −27 nm. At high magnification, Scherzer can be seen as a local maximum in the contrast variation of a beam-stable amorphous film.

After focusing, the beam blanking device is turned on and the sample stage mechanism allowed to relax, damping out residual mechanical drift. Finally, the 'PHOTO' button is pressed using a second beam blanking time of 10 s to avoid vibrations from the motion of the phosphorus screen and advancing film. After exposure, a second image is typically taken of the same region with a somewhat longer exposure time for better determination of the sample position as well as for defocus and sample thickness calibration.

HREM imaging of fibrous materials is more complicated than that of polymer films or of single crystals supported on a carbon substrate. The problem is that a suitable area for focusing must be found every time a new region of the sample is imaged. This means that the 'FOCUS' conditions must be adjusted every time an image is taken. Further, it is important to focus on an area as near as possible to the region of interest because of the possible non-planarity of the sample over large distances. Durst and Voigt-Martin use a sprinkling of carbon particles to assist in proper focusing of the microscope[59].

One of the more insidious problems encountered during HREM imaging is the effect of sample drift. Drift

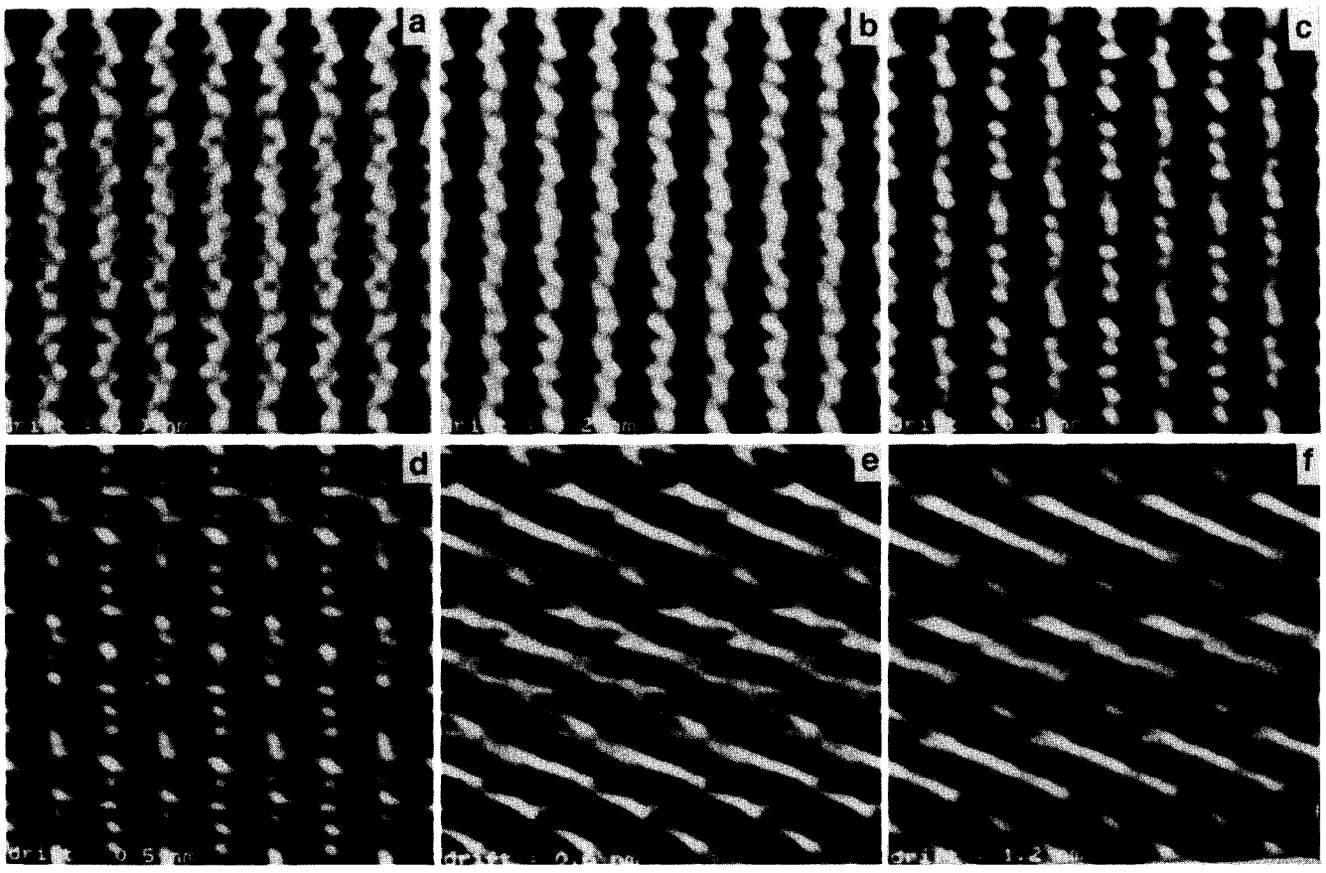


**Figure 8** Effect of sample drift on simulated images. Note that, even for reasonably large sample drifts, the proper orientation of the primary fringes is still preserved. Only when the drift becomes greater than that of the primary periodicities are the features completely obscured. Images are shown for drifts of (a) 0.0 nm, (b) 0.2 nm, (c) 0.4 nm, (d) 0.5 nm, (e) 0.6 nm and (f) 1.2 nm

of more than 0.2 nm during the exposure can easily ruin a micrograph. The obscuring effect of drift is shown via the simulations in *Figure 8*, which predict the effect of uniform drift on an HREM image of PBZO. Image features due to drift can easily be distinguished from actual features characteristic of sample structure by examination of the optical diffraction pattern of the HREM image. Samples that have drifted during exposure show a loss in the intensity of the $\sin^2[\chi(k)]$ defocus rings at higher frequencies in the direction of drift. The amount of drift can be estimated from the width of the intensity attenuation. It is, of course, important that the oriented 'fringes' that can occasionally be seen in drifted images are not interpreted as representative of the sample microstructure.

*Sample thickness determination*

An important parameter for interpreting HREM images is the sample thickness. An accurate estimate of the thickness is necessary to determine whether features that are close to each other in projection are actually close together in the film itself, or perhaps arise from regions as far apart as the top or bottom of the film. As the sample thickness increases, the likelihood of feature superposition becomes large and the images become more difficult to interpret.

It is possible to estimate the thickness of a thin film of organic material by mass thickness contrast. In mass thickness contrast, the transmitted electron intensity $I$ is related to the incident electron intensity $I_0$ by the relationship[79]:

$$I/I_0 = \exp(-S_p \rho t) \tag{20}$$

where $S_p$ is the effective mass thickness cross-section, $\rho$ is the density and $t$ is the thickness. The effective mass thickness cross-section $S_p$ describes the amount of scattering outside of the field limiting aperture and depends only on the size of the aperture $A_1$ and the operating voltage $E_0$. $S_p$ for a given $A_1$ and $E_0$ may be determined by measuring $I$ and $I_0$ for a sample of known $t$ and $\rho$.

It should be noted that this relationship is valid only for a nearly focused objective lens. This is because at zero focus there is no phase contrast for large objects ($T$ in equation (4) goes to 0 for small $k$). Experimentally, for a focus range of $\pm 4000$ nm near Scherzer focus, the ratio of transmitted beam intensity at a sample to that of vacuum varies by only 5% (*Figure 9*). This is well within the range of focusing used in typical HREM imaging (typically less than $\pm 400$ nm). However, it should be noted that significant errors (25% or more) can occur for highly defocused images.

The $S_p$ values for the JEOL 2000 FX were determined by using calibrated polystyrene spheres of diameter 109 nm on a thin (approximately 10 nm) polystyrene support film. The photographic film used was Kodak SO-163, developed in straight D-19 for 12 min at room temperature. Optical densities were measured using a

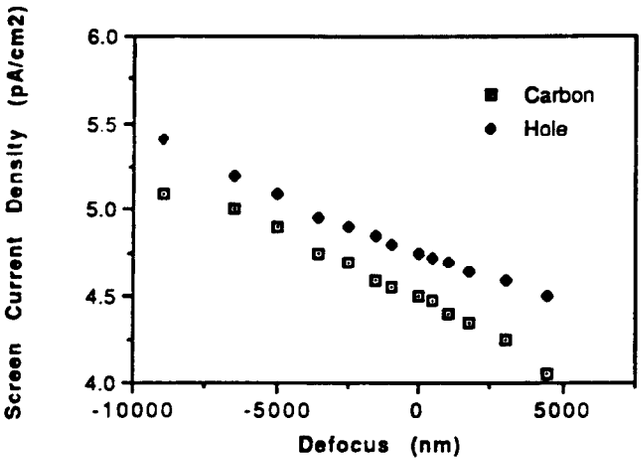


**Figure 9** Beam intensity of a holey carbon film compared to vacuum as a function of objective lens defocus. For defocus ranges near zero, the intensity difference between sample and vacuum varies by only 5%. For larger defocus, the error can be more than 25%

plate microdensitometer calibrated with an optical density step wedge.

*Table 2* lists the effective mass thickness cross-sections for different objective apertures in the JEOL 2000 FX using 200 kV electrons. From this calibration the thickness of an unknown sample may be determined by comparing the optical density of the sample to that of a hole. Using $\rho = 1.6\,g\,cm^{-3}$, the density of PBZT, it is seen that under these imaging conditions it would require 240 nm of PBZT to cause a factor of 2 (100%) decrease in the optical density.

The optical density of a typical substrate-free sample on an HREM image is only 7% less than the neighbouring vacuum using no objective aperture. This corresponds to a sample thickness of 24 nm. This approach to thickness determination is complicated by the presence of a thin support film, which will introduce fluctuations in the local background intensity.

*Photographic details*

HREM images of polymers typically involve spacings from 0.35 to 2.5 nm obtained at magnifications from 25 000 to 250 000 ×. This corresponds to distances on the film from 25 to 300 $\mu$m. An optical density on the negative of 0.5–1.0 is typically used. For Kodak SO-163 electron image film, it was experimentally determined that an optical density of 1.0 required an illumination dose of $10\,pC\,cm^{-2}$.

Because of the small size of features on low-dose micrographs, it is not simple to examine the HREM negatives directly and see 'fringes'. Even with a 10 × eyepiece, it is a difficult matter to see fringes on low-dose micrographs. For assessing whether an HREM negative has fringes or not, it is quickest and easiest to examine the negative by laser light scattering on an optical bench.

*Optical bench*

The optical bench provides a quick route for analysing micrographs by light scattering. Illumination of the negative with a laser beam enables the scattering pattern of the image to be obtained. Essentially, this technique is a rapid means of taking an analogue Fourier transform of a local area of the micrograph. The optical transform can be calibrated with a micrograph of a known object. A convenient sample for this purpose is the 0.34 nm spacing of turbostratic graphite.

Once an area of interest is located on a HREM negative, the optical diffraction pattern may be recorded on T-55 Polaroid film. Enlargement of the area of interest is performed using a standard film enlarger, typically with a 50 mm lens. Large *f*-stops (*f*22) are used in order to have the best possible depth of focus. This might require an exposure time on the print paper of up to 5 min or more. Precise focusing of the enlarger can be accomplished with a periscope device, which enables focusing directly on the film grain.

Often, the capabilities of an enlarger (typical maximim magnification of 20 ×) are insufficient or a microdensitometer scan of the image is desired. In these cases, an intermediate negative can be used to provide a magnified negative image suitable for further enlargement or for scanning on a densitometer. Intermediate negatives may also be prepared using Kodak SO-163 electron image film. Careful focusing using a large *f*-stop is critical to ensure a high-quality intermediate.

*Digital imaging*

The analysis of HREM images is facilitated by digital image analysis. Images can be digitized via a two-dimensional scanning microdensitometer or by a video or CCD camera coupled to a computer with a frame-grabbing board. Software packages for image analysis include SEMPER[29] and the public-domain program IMAGE[80].

With image processing software packages it is possible to perform a variety of operations including two-dimensional discrete fast Fourier transforms (*FFT*) to analyse the frequency information in the HREM images and relate these to the expected spacings in the sample. It is also possible to quantify contrast variations in optical density units by comparison to calibration standards. One can also digitally filter and reconstruct images to highlight specific regions containing a certain periodicity of interest. This is essentially the digital analogue of DF imaging.

More eleborate numerical algorithms for digital image reconstruction of low-dose HREM images using maximum-entropy approaches have also been proposed[81]. HREM represents a particular challenge for image reconstructions, since both the frequency and position information needs to be retained. However, it has been shown that such methods can compromise the integrity of the frequencies in the data when applied in real space, and can alter position information when applied in frequency space[82].

**Table 2** Mass thickness cross-sections for a JEOL 2000 FX Transmission Electron Microscope at 200 kV

| Aperture diameter ($nm^{-1}$) | $S_p$ ($m^2\,mg^{-1}$) |
|---|---|
| none | 0.0018 |
| 6.1 | 0.0020 |
| 4.3 | 0.0024 |
| 2.6 | 0.0031 |

Improvements in image detection technologies are always an item of continued interest. High-quality results can be obtained with metal halide electron image film. Dynamic images can be obtained on a YAG crystal with an image intensifier fibre-optically coupled to a video camera. Improvements in sensitivity and linearity of response require CCD cameras, but these do not respond as quickly as video rate systems. Despite computational advances, experience has shown that for single-image acquisition and archiving all of the digital technologies currently available have significantly less information storage capacity and convenience than conventional metal halide films.

*Recent and future developments*

By deflecting the beam at a specific angle and rotating it around the optical axis during exposure, it is possible to generate a hollow-cone illumination that can improve the theoretical resolution of the microscope by a factor of approximately 2 (ref. 76). In order for this procedure to be effective, it is necessary that the voltage centring and astigmatism be precisely corrected. To our knowledge this approach has not yet been applied to the HREM imaging of beam-sensitive samples.

There are now two different proven approaches for electron energy filtering technologies for high-voltage beams in the TEM. These include the post-column energy filter, which can be attached to an existing microscope[83], and the in-column approach, which requires a curved sector lens[84]. The use of energy filtering for obtaining improved contrast in HREM has been reported[85]. These technologies have significant potential for improving the imaging capabilities of samples with low atomic number.

Developments in electron sources have led to field-emission guns for the TEM with significantly improved brightness and coherence. These sources have made it possible to observe the flux lattice in superconductors and magnetic thin films[86]. It might one day be possible to image flux lines or charge-carrier transport in conductive or photoconductive polymer thin films.

In closing, we consider the theoretical instrumental capabilities that would be required to resolve variations in the symmetry of the electronic distribution around the atom nucleus. In other words, what resolution would be required to resolve molecular-orbital hybridization around the carbon atom by HREM? These variations are an important feature of many polymer systems, and the possibility of revealing changes in local electron distribution would provide fascinating new insight about molecular structure.

To resolve this question, we examined the scattering behaviour of diamond, which is known to exhibit a small but detectable amount of scattering at the (222) position in reciprocal space, even though this reflection should be systematically absent if the electrons were symmetrically arranged about the carbon nucleus. According to Dawson[87], in X-ray diffraction the intensity of the (222) reflection is 0.7% that of the (111).

There is currently no commercially available software package that has the capability to model non-spherically symmetric electron distribution about the atom. Further complicating the matter is the fact that the non-spherically symmetric scattering factors are not well known. We therefore required a scheme to approximate a non-spherically symmetric tetrahedrally coordinated $sp^3$-hybridized carbon atom using available analysis packages. We accomplished this task by using a discretized atom approximation: a helium atom and four hydrogen atoms were substituted for each carbon atom. With the hydrogen atoms superposed on the helium at the origin, the intensity of the (222) reflection was zero, as also observed for single carbon atoms. We then translated the four hydrogen atoms away from the helium atom in a tetrahedrally symmetric manner until the theoretically calculated intensity of the (222) reflection was the same as that observed experimentally for diamond. This was achieved at a displacement of 0.02 nm (0.2 Å) away from the origin. The projected potential of the diamond crystal with spherically symmetric carbons and the discretized atom approximation with a helium and four hydrogens are shown in *Figure 10*.

If we presume that this dimension (0.02 nm) corresponds to the instrumental resolution that would be required to observe molecular-orbital hybridization, then from the expression for resolution derived earlier ($d = 0.66(C_s\lambda^3)^{1/4}$) we find that a spherical aberration coefficient of 0.2 $\mu$m would be required with a 400 kV instrument ($\lambda = 1.6$ pm). This is three orders of magnitude smaller than any objective pole piece currently available (with lens designs now only approaching $C_s = 0.2$ mm at best). This demonstrates the considerable technical challenges required for continued improvements in TEM resolution with new instrumentation. It has been argued that considerable

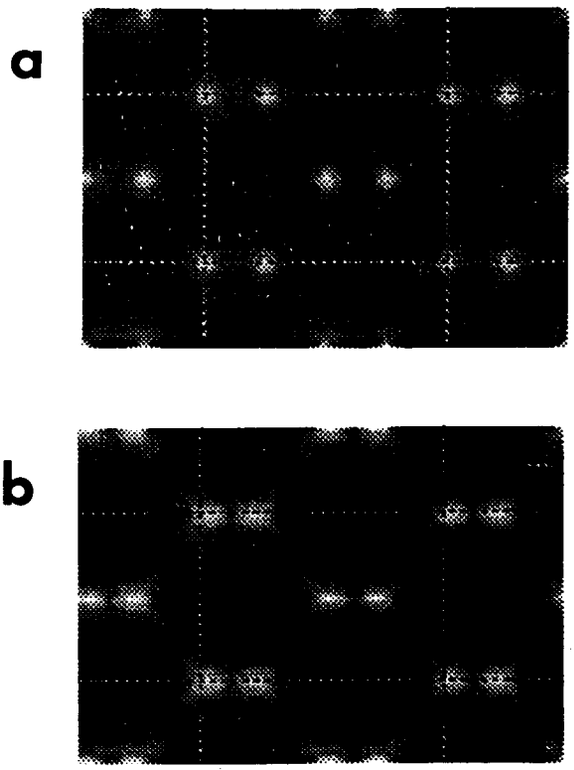


**Figure 10** (a) Projected electron potential for diamond with spherically symmetric carbon atoms. (b) Projected electron potential for discretized atom approximation in which each carbon atom is replaced by one helium atom and four hydrogen atoms tetrahedrally arranged in a manner consistent with the $sp^3$ molecular-orbital hybridization. The hydrogens are displaced 0.02 nm away from the central helium. The intensity of scattering of the (222) reflection of this model structure is consistent with that seen by experiment. A resolution of 0.02 nm at 400 kV would require an objective lens with $C_s = 0.2$ $\mu$m

advances could arise from dedicated efforts towards significant miniaturization of the TEM and SEM[88]. It may eventually be possible to use solid-state silicon micromachining to construct arrays of small microscopes for high-resolution, local imaging capabilities unprecedented by current technologies.

## SUMMARY

We have discussed in detail the physics of HREM image formation and have shown what is to be expected when imaging crystalline polymer microstructures. We found that, while the specific details corresponding to intramolecular structure could not be faithfully interpreted, it was possible to associate well defined periodic fringes with similarly well ordered areas of molecular packing in the sample. For rigid extended-chain polymers, equatorial fringes correspond to a direct mapping of the local molecular orientation. Axial registry between molecules is manifest as fringes nominally perpendicular to the fibre axis. The perfection, extent and contrast of these fringes all depend on the local molecular order.

In addition, we have described practical information that should be helpful for those wishing to attempt low-dose HREM on polymer systems of their own specific interest. While such studies have only recently begun, interesting new information about the details of solid-state polymer architecture has been obtained. Similar success is no doubt possible for a variety of other interesting macromolecular systems.

## REFERENCES

1 Spence, J. C. H. 'Experimental High Resolution Electron Microscopy', 2nd Edn., Oxford University Press, Oxford, 1988
2 Amelinckx, S. 'High resolution electron microscopy in materials science', in 'Examining the Submicron World' (Eds. R. Feder, J. Wm McGowan, and D. M. Shinozaki), NATO ASI Ser. B, Physics, Vol. 137, Plenum, New York, 1986
3 Fujita, F. E. and Hirabayashi, M. 'High-resolution electron microscopy', in 'Microscopic Methods in Metals' (Ed. U. Gonser), Topics in Current Physics, Vol. 40, Springer-Verlag, Berlin, 1986
4 Buseck, P. R., Cowley, J. M. and Eyring, L. (Eds.) 'High-Resolution Transmission Electron Microscopy and Associated Techniques', Oxford University Press, Oxford, 1988
5 Kobayashi, T. and Isoda, S. *J. Mater. Chem.* 1993, **3**(1), 1
6 Martin, D. C. and Thomas, E. L. *Mater. Res. Soc. Bull.* 1987, **XII**(8), 27
7 Tsuji, M. in 'Comprehensive Polymer Science' (Ser. Eds. C. C. Booth and C. Price), Vol. 1 (Eds. G. Allen and J. C. Bevington), Pergamon, Oxford, 1989
8 Voigt-Martin, I. G., Krug, H. and Van Dyck, D. *J. Phys. Fr.* 1990, **51**, 2347
9 Martin, D. C., Wilson, P. M. and Liao, J. *Polym. Prepr.* 1992, **33**(1), 245
10 DeRosier, D. J. and Klug, A. *Nature* 1968, **217**, 130
11 Hirsch, P. B., Howie, A., Nicholson, R. B., Pashley, D. W. and Whelan, M. J. 'Electron Microscopy of Thin Crystals', Butterworth, London, 1965
12 Moodie, A. F. *Z. Naturforsch.* 1972, **27a**, 437
13 Lynch, D. F., Moodie, A. F. and O'Keefe, M. *Acta Crystallogr. (A)* 1975, **31**, 300
14 Cowley, J. M. and Moodie, A. F. *Acta Crystallogr.* 1957, **10**, 609
15 Cowley, J. M. in 'High Resolution Transmission Electron Microscopy and Associated Techniques' (Eds. P. Buseck, J. Cowley and L. Eyring), Oxford University Press, Oxford, 1989
16 Tsuji, M. and St John Manley, R. *J. Microsc.* 1983, **130**(1), 93
17 Dainty, J. C. and Shaw, R. 'Image Science: Principles, Analysis, and Evaluation of Photographic-type Imaging Processes', Academic Press, London, 1974
18 Shepp, A. in 'Imaging Processes and Materials', Neblettes 8th Edn. (Eds. J. Sturge, V. Walworth and A. Shepp), Van Nostrand Reinhold, New York, 1989
19 Pradere, P., unpublished, 1988
20 Scherzer, O. *J. Appl. Phys.* 1949, **20**, 20
21 Ourmazd, A. and Spence, J. C. H. *Nature* 1987, **329**, 425
22 Huxford, N. P., Eaglesham, D. J. and Humphreys, C. J. *Nature* 1987, **329**, 812
23 Mott, N. F. and Massey, H. S. W. 'The Theory of Atomic Collisions', 3rd Edn., Clarendon, Oxford, 1965, pp. 86–112
24 Peng, L.-M. and Cowley, J. M. *Acta Crystallogr. (A)* 1988, **44**, 1
25 Shimamura, K., Minter, J. R. and Thomas, E. L. *J. Mater. Sci. Lett.* 1983, **2**, 54
26 Adams, W. W., Kumar, S., Martin, D. C. and Shimamura, K. *Polym. Commun.* 1989, **30**, 285
27 Martin, D. C. and Thomas, E. L. *Macromolecules* 1991, **24**, 2450
28 Adams, W. W. and Fratini, A. *Am. Cryst. Assoc. Abstr.* 1985, **13**, 72
29 SEMPER is available from Synoptics Ltd, Nashua, NH
30 Pradere, P. and Thomas, E. L. 'Proceedings of the 47th Annual Meeting of the Electron Microscopy Society of America' (Ed. G. W. Bouley), San Francisco Press, San Francisco, 1989, p. 342
31 Bassett, G. A. and Keller, A. as cited by Keller, A. *Kolloid-Z.* 1969, **231**, 386
32 Dobb, M. G., Hindeleh, A. M., Johnson, D. J. and Saville, B. P. *Nature* 1975, **253**, 189
33 Northolt, M. G. *Eur. Polym. J.* 1974, **10**, 799
34 Bennett, S. C., Dobb, M. G., Johnson, D. J., Murray, R. and Saville, B. P. 'High resolution studies of electron-beam sensitive polymers', EMAG Proc., 1975, pp 329–32
35 Dobb, M. G., Johnson, D. J. and Saville, B. P. *J. Polym. Sci., Polym. Phys. Edn.* 1977, **15**, 2201
36 Read, R. T. and Young, R. J. *J. Mater. Sci. Lett.* 1981, **16**, 2922
37 Read, R. T. and Young, R. J. *J. Mater. Sci.* 1984, **19**, 327
38 Yeung, P. H. J. and Young, R. J. *Polymer* 1986, **27**, 202
39 Tsuji, M., Roy, S. K. and St John Manley, R. *Polymer* 1984, **25**, 1573
40 Tsuji, M., Uemura, A., Ohara, M., Kawaguchi, A., Katayama, K. and Petermann, J. *Sen-I Gakkaishi* 1986, **42**(10), 92
41 Chanzy, H., Folda, T., Smith, P., Gardner, K. and Revol, J. F. *J. Mater. Sci. Lett.* 1986, **5**, 1045
42 Uemura, A., Tsuji, M., Kawaguchi, A. and Katayama, K. *J. Mater. Sci.* 1988, **23**, 1506
43 Giorgio, S. and Kern, R. *J. Polym. Sci., Polym. Phys. Edn.* 1984, **22**, 1931
44 Revol, J.-F. and St John Manley, R. *J. Mater. Sci. Lett.* 1986, **5**, 249
45 Chanzy, H. D., Smith, P., Revol, J.-F. and St John Manley, R. *Polym. Commun.* 1987, **23**, 133
46 Sugiyama, J., Harada, H., Fujiyoshi, Y. and Uyeda, N. *Mokuzai Gakkaishi* 1984, **30**(1), 98
47 Sugiyama, J., Harada, H., Fujiyoshi, Y. and Uyeda, N. *Planta* 1985, **166**, 161
48 Revol, J.-F. *J. Mater. Sci. Lett.* 1985, **4**, 1347
49 Kuga, S. and Brown, R. M. Jr *Polym. Commun.* 1987, **28**, 311
50 Revol, J., Chanzy, H. D., Deslandes, Y. and Marchessault, R. H. *Polymer* 1990, **30**, 1973
51 Kawaguchi, A., Isoda, S., Petermann, J. and Katayama, K. *Colloid Polym. Sci.* 1984, **262**, 429
52 Zhou, X., Marks, T. J. and Carr, S. H. *Mol. Cryst. Liq. Cryst.* 1985, **118**, 357
53 Tsuji, M., Ph.D. Thesis, Institute for Chemical Research, Kyoto University, 1981
54 Tsuji, M., Isoda, S., Ohara, M., Kawaguchi, A. and Katayama, K. *Polymer* 1982, **23**, 1568
55 Pradere, P. and Thomas, E. L. *Phil. Mag. (A)* 1990, **60**, 177
56 Fryer, J. R. 'Crystallization and lattice resolution of a straight chain paraffin n-$C_{36}H_{74}$ and its adducts', presented at EMAG, Cambridge, September 1981, Inst. Phys. Conf. Ser. No. 61, Bristol, Institute of Physics, 1982, Ch. 1, pp. 19–22
57 Fryer, J. R., Hann, R. A. and Eyres, B. L. *Nature* 1985, **313**(6001), 382
58 Fryer, J. R. and Dorset, D. L. *J. Microsc.* 1987, **145**(1), 61
59 Durst, H. and Voigt-Martin, I. G. *Makromol. Chem. Rapid Commun.* 1986, **7**, 785
60 Voigt-Martin, I. G. and Durst, H. *Macromolecules* 1989, **22**, 168
61 Voigt-Martin, I. G., Garbella, R. W. and Schumacher, M. *Macromolecules* 1992, **25**, 961
62 Martin, D. C. and Thomas, E. L. *J. Mater. Sci.* 1991, **26**, 5171

63 Martin, D. C. and Thomas, E. L. *Phil. Mag.* (*A*) 1991, **64**(4), 903
64 Pradere, P. and Thomas, E. L. *Macromolecules* 1990, **23**, 4954
65 Masse, M. A., Martin, D. C., Thomas, E. L., Karasz, F. E. and Petermann, J. H. *J. Mater. Sci.* 1990, **25**, 311
66 Martin, D. C., Berger, L. L. and Gardner, K. H. *Macromolecules* 1991, **24**, 3921
67 Ojeda, J. R. and Martin, D. C. *Macromolecules* 1993, **26**, 6557
68 Wilson, P. M. and Martin, D. C. *J. Mater. Res.* 1992, **7**(11), 3150
69 Liao, J. and Martin, D. C. *Science* 1993, **260**, 1489
70 Lieser, G., Wang, W., Albrecht, C., Schwiegk, S., Rehahn, M. and Wegner, G. *Polym. Prepr.* 1992, **33**(1), 294
71 Hudson, S. D., Lovinger, A. J., Gomez, M. A., Lorente, J., Marco, C. and Fatov, J. G. *Macromolecules* 1994, **27**, 3357
72 Grubb, D. H. *J. Mater. Sci.* 1974, **9**, 1715
73 Kumar, S. and Adams, W. W. *Polymer* 1990, **31**, 15
74 Tomita, M., Hashimoto, H., Ikuta, T., Endoh, H. and Yokata, Y. *Ultramicroscopy* 1985, **16**, 9
75 Saxton, W. O., Smith, D. J. and Erasmus, S. J. *J. Microsc.* 1983, **130**(2), 187
76 Kunath, W., Zemlin, F. and Weiss, K. *Optik* 1987, **76**(4), 122
77 Pradere, P., personal communication, 1989
78 Krivanek, O. L. 'Practical high-resolution electron microscopy', in 'High Resolution Transmission Electron Microscopy and Associated Techniques' (Eds P. Buseck, J. Cowley and L. Eyring), Oxford University Press, Oxford, 1989
79 Misell, D. L. and Burdett, I. D. J. *J. Microsc.* 1977, **109**(2), 171
80 IMAGE was developed at the National Institutes of Health and is available by remote FTP from zippy.nimh.nih.gov. At the University of Michigan we use a version modified for Hartley transforms by A. Reeves of Dartmouth College and further modified by J. Mansfield and D. Crawford of the University of Michigan
81 Anderson, D. M., Martin, D. C. and Thomas, E. L. *Acta Crystallogr.* (*A*) 1989, **45**, 686
82 Martin, D. C., Schaffer, K. R. and Thomas, E. L. in 'Electron Crystallography of Organic Molecules' (Eds J. R. Fryer and D. L. Dorset), NATO ASI Ser., Kluwer Academic, Dordrecht, 1991, pp. 129–145
83 Krivanek, O. L., Gubbens, A. J., Dellby, N. and Meyer, C. E. 'Proceedings of the 50th Annual Meeting of the Electron Microscopy Society of America', San Francisco Press, San Francisco, 1992, pp. 1192–1193
84 Bihr, J. 'Proceedings of the 49th Annual Meeting of the Electron Microscopy Society of America', San Francisco Press, San Francisco, 1991, pp. 354–355
85 Hashimoto, H., Makira, Y. and Nagaoka, N. 'Proceedings of the 50th Annual Meeting of the Electron Microscopy Society of America', San Francisco Press, San Francisco, 1992, pp. 1194–1195
86 Yoshida, T., Matsuda, T. and Tonomura, A. 'Proceedings of the 50th Annual Meeting of the Electron Microscopy Society of America', San Francisco Press, San Francisco, 1992, pp. 68–69
87 Dawson, B. *Proc. R. Soc.* (*A*) 1966, **298**, 266
88 Crewe, A. 'Proceedings of the 51st Annual Meeting of the Electron Microscopy Society of America', San Francisco Press, San Francisco, 1993, pp. 2–3